The STACEE Ground-Based Gamma-Ray Detector

D. M. Gingrich, L. M. Boone, D. Bramel, J. Carson, C. E. Covault, P. Fortin, D. S. Hanna, J. A. Hinton, A. Jarvis, J. Kildea, T. Lindner, C. Mueller, R. Mukherjee, R. A. Ong, K. Ragan, R. A. Scalzo, C. G. Théoret, D. A. Williams, and J. A. Zweerink

***Abstract*—We describe the design and performance of the Solar Tower Atmospheric Cherenkov Effect Experiment (STACEE) in its complete configuration. STACEE uses the heliostats of a solar energy research facility to collect and focus the Cherenkov photons produced in gamma-ray induced air showers. The light is concentrated onto an array of photomultiplier tubes located near the top of a tower. The large Cherenkov photon collection area of STACEE results in a gamma-ray energy threshold below that of previous ground-based detectors. STACEE is being used to observe pulsars, supernova remnants, active galactic nuclei, and gamma-ray bursts.**

***Index Terms*—Cherenkov detectors, coincidence detection, cosmic rays, delay circuit, Gamma-ray astronomy detectors, triggering.**

I. Introduction

GAMMA-RAY astronomy has become a very exciting area of research. Since 1991 the field has rapidly expanded due to the increased quantity and quality of data as well as an improved theoretical understanding of the related astrophysics. The thrust in the field was primarily initiated by NASA's Compton Gamma Ray Observatory (CGRO) and the ground-based detectors that ran concurrently. The Energetic Gamma Ray Experiment Telescope (EGRET) aboard the CGRO produced a catalog of over 200 high-energy point sources [1]. Since space-borne instruments are by necessity small detectors, they are only able to detect sources below about 10 GeV due to flux limitations. To increase the energy range, ground-based detectors must be used.

Almost all ground-based gamma-ray detectors use the atmospheric Cherenkov technique. Typical Cherenkov telescopes detect gamma rays by using large steerable mirrors to collect, focus, and image the Cherenkov light produced by the relativistic electrons resulting from the interactions of high-energy gamma rays in the upper atmosphere. This Cherenkov light is distributed on the ground in a circular pool with a diameter from 200 m to 300 m. The size of the light pool is almost independent of the primary gamma-ray energy, but the Cherenkov photon density scales linearly with the primary gamma-ray energy. Imaging Cherenkov telescopes have a very large collection area relative to satellite detectors, and need only capture a part of the total Cherenkov light pool to detect the primary gamma ray. This gives rise to a low-energy threshold of about 300 GeV.

The energy range between EGRET and imaging Cherenkov telescopes remained unexplored until recently because no detectors were sensitive to the energy region between 10 GeV and 300 GeV. The wavefront sampling technique is a variant of the imaging Cherenkov technique whereby the collecting mirror is synthesized by an array of large steerable mirrors (heliostats) at a central-tower solar energy installation. The large effective area of the collecting mirror allows one to trigger at lower photon densities, and therefore lower primary gamma-ray energies. STACEE is a wavefront sampling detector designed to lower the threshold of ground-based gamma-ray astronomy to approximately 50 GeV, near the upper limit of satellite detectors [2]. Three other projects of a similar nature have also been built: CELESTE [3], Solar-2/CACTUS [4], and GRAAL [5].

STACEE is investigating established and putative gamma-ray sources. One of its principle aims is to follow the spectra of active galactic nuclei (AGN) out to energies beyond that of EGRET measurements to determine where the spectra deviate from a power law. Many EGRET sources are not detected by imaging telescopes despite the fact that a simple extrapolation of EGRET spectra are often well within the sensitivities of such detectors. We must then conclude that the spectra are somehow attenuated in the 10 GeV to 300 GeV energy region. This effect could be due to cutoff mechanisms intrinsic to the source, or to absorption effects between the source and the detector. A likely absorption mechanism is pair production, wherein the high-energy gamma ray combines with a low-energy photon (optical

Manuscript received November 15, 2004; revised April 21, 2005. This work was supported in part by the National Science Foundation, the Natural Sciences and Engineering Research Council, Fonds Québécois de la Recherche sur la Nature et les Technologies, the Research Corporation, and the California Space Institute.

D. M. Gingrich is with the Centre for Subatomic Research, University of Alberta, Edmonton, AB T6G 2N5, Canada and TRIUMF, Vancouver, BC V6T 2A3, Canada (e-mail: gingrich@ualberta.ca).

L. M. Boone was with the Santa Cruz Institute for Particle Physics, University of California, Santa Cruz, CA 95064 USA. He is now with the Department of Physics, The College of Wooster, Wooster, OH 44691 USA.

D. Bramel and R. Mukherjee are with the Department of Physics and Astronomy, Barnard College and Columbia University, New York, NY 10027 USA.

J. Carson, A. Jarvis, R. A. Ong, and J. A. Zweerink are with the Department of Physics and Astronomy, University of California, Los Angeles, CA 90095 USA.

C. E. Covault is with the Department of Physics, Case Western Reserve University, Cleveland, OH 44106, USA.

P. Fortin, D. S. Hanna, J. Kildea, T. Lindner, C. Mueller, and K. Ragan are with the Department of Physics, McGill University, Montreal, QC H3A 2T8, Canada.

J. A. Hinton was with the Enrico Fermi Institute, University of Chicago, Chicago, IL 60637 USA. He is now with the Max-Planck-Institut für Kernphysik, D-69029 Heidelberg, Germany.

R. A. Scalzo was with the Enrico Fermi Institute, University of Chicago, Chicago, IL 60637 USA. He is now with the Lawrence Berkeley National Laboratory, Berkeley, CA 94720 USA.

C. G. Théoret was with the Department of Physics, McGill University, Montreal, QC H2A2T8, Canada. He is now with the Laboratoire de Physique, Collége de France, F-75231 Paris CEDEX 05, France.

D. A. Williams is with the Santa Cruz Institute for Particle Physics, University of California, Santa Cruz, CA 95064 USA.

Digital Object Identifier 10.1109/TNS.2005.855705

Fig. 1. National Solar Thermal Test Facility at Sandia National Laboratories in Albuquerque, NM. The heliostat field covers an area of about 160 m by 260 m.

or infrared) from the extragalactic background radiation field. Absorption by pair production thus makes gamma-ray measurements of distant sources an indirect method of measuring the integrated light from past star formation.

II. STACEE Detector

The STACEE detector was in a state of development from 1997 to 2002. Stages of the construction were followed by observing periods using the partially completed detector. Since spring of 2002, the detector has been fully completed and is being used for astrophysical observations.

STACEE uses the National Solar Thermal Test Facility (NSTTF), which is situated at Sandia National Laboratories in Albuquerque, New Mexico (see Fig. 1). Since the NSTTF is a solar research facility and STACEE observes at night, there is no significant interference between the two programs. Sixty-four of the 220 heliostats are used during clear moonless nights to collect Cherenkov light from air showers and direct it onto five secondary mirrors located near the top of a 61 m tower. The secondary mirrors focus the Cherenkov light into groups of photomultiplier tubes (PMTs) such that each PMT views a single heliostat. Optical concentrators widen the aperture of each PMT and restrict its field of view to reduce the number of night-sky background photons detected. Signals from the PMTs are amplified and routed to a control room where high-speed electronics measure the charge and relative arrival times of the PMT pulses. Signals above threshold are discriminated and processed by a delay and coincidence trigger system.

A. Heliostats

Fig. 2 shows the heliostats in the NSTTF field that are used by STACEE. The choice of the 64 heliostats used in STACEE is based on the desire to uniformally sample the Cherenkov light pool expected from a shower impacting near the center of the array, while not crowding the PMTs in the image plane. The collective area of the 64 heliostats is over 2300 m^2.

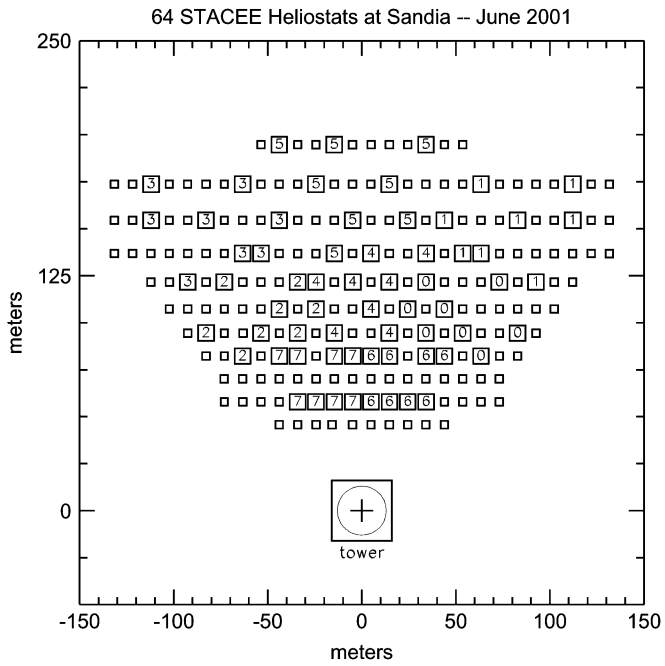

Fig. 2. Map of the heliostats in the National Solar Thermal Test Facility field used by STACEE. The STACEE heliostats are numbered according to the trigger cluster to which they belong. Clusters 0 and 1 correspond to the "east" camera, clusters 2 and 3 correspond to the "west" camera, clusters 4 and 5 correspond to the "north" camera, cluster 6 corresponds to the "southeast" camera, and cluster 7 corresponds to the "southwest" camera.

Each heliostat has a mirror area of 37 m^2, and consists of 25 square facets mounted on a steel frame. Each facet is a 1.2 m by 1.2 m square of back-surfaced aluminized glass glued onto a thin metal sheet. The facets are distorted into approximately parabolic shapes with the focus set to be equal to the distance to the tower. Each facet can be separately aligned so that their beams overlap at the tower.

The entire heliostat is mounted in a yoke structure which allows rotation in azimuth and elevation angles. The motion is achieved with two electric motors, each of which is controlled by the NSTTF central computer using 13-bit encoders.

Facet alignment is checked and tuned using images of the Sun projected onto the tower near solar noon (sunspots). The Sun is a good diagnostic since its angular size (0.5°) is very similar to that of a Cherenkov shower. The absolute pointing of each heliostat is calibrated to an accuracy of 0.05° using drift scans of bright stars.

B. Secondary Mirrors

Cherenkov photons are reflected by the heliostats onto five secondary mirrors located near the top of the central tower (see Fig. 3). Sixteen heliostats in the north, 16 heliostats in the east, and 16 heliostats in the west regions of the field (see Fig. 2) are viewed by three independent mirrors located 49 m above the base of the tower. Similarly, eight heliostats in the southeast and eight heliostats in the southwest of the field (see Fig. 2) are viewed by two independent mirrors 37 m above the base of the tower.

The three secondary mirrors at the 49 m level are spherical with a nominal diameter of 1.9 m and a focal length of 2.0 m. Each is composed of seven identical hexagonal facets

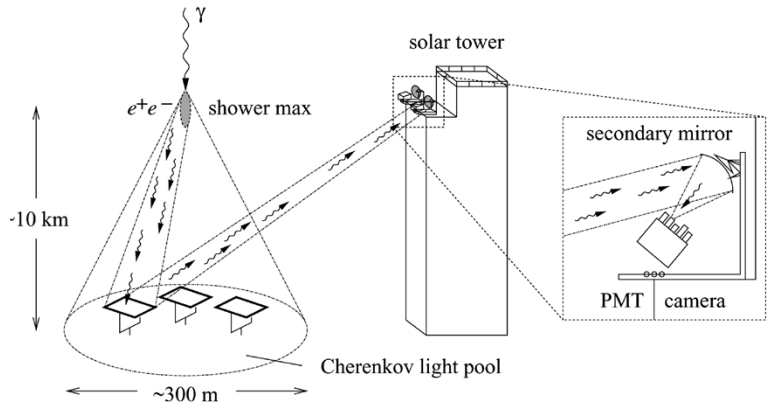

Fig. 3. Concept of the solar tower Cherenkov detection of gamma-ray air showers (not to scale).

made from front-surfaced aluminized glass in order to retain a high reflectivity at ultraviolet wavelengths, where most of the Cherenkov light from air showers is produced. The two secondary mirrors at the 37 m level are single spherical mirrors with a diameter of 1.1 m and a focal length of 1.1 m.

The secondary mirrors focus the light from the heliostats, which arrives as a wide beam, onto phototube assemblies fixed in position at the focal plane. The optics are such that each heliostat is mapped onto a single PMT channel. This one-to-one mapping is vital for pattern recognition, which is used in trigger formation and background suppression.

C. Cameras

The final stage in the STACEE optics chain is the camera. There is one camera for each secondary mirror. The cameras at the 49 m level consist of 16 PMT assemblies and the cameras at the 37 m level of eight PMT assemblies each. Each PMT assembly consists of a PMT and light concentrator enclosed in a canister. The PMT canisters are mounted in cylindrical sleeves attached to an azimuthal-elevation mounting system secured to a slotted plate. With this system, it is possible to position the PMT canisters anywhere laterally on the slotted plate and to adjust the orientation of the canisters such that they point to the center of the secondary mirror.

The light concentrators are Dielectric Total Internal Reflection Concentrators (DTIRCs) [6] made from solid UV-transparent acrylic. These are nonimaging devices which use total internal reflection to transport light from the front surface to the exit aperture. The light from a circular area of 11 cm diameter is concentrated to an exit diameter of less than 4 cm. Only light from a given angular range can reach the exit aperture, so the DTIRCs have the added feature of being able to define the field of view of the PMT.

For far-away heliostats, spherical aberration distorts the shape of the image and produces a long coma tail, large enough in some cases to overlap the apertures of other DTIRCs. While somewhat troublesome for certain calibration activities, this overlap is not expected to present a difficulty during normal astronomical observations; the arrival times of a Cherenkov wavefront at the apertures of adjacent DTIRCs usually differ by several tens of nanoseconds. Any crosstalk photons will therefore lie outside the coincidence trigger window, and will not contribute to the trigger.

D. Photomultiplier Tubes

STACEE uses the Photonis XP2282B photomultiplier tube with a borosilicate window and a VD182K/C transistorized voltage divider. This tube has a good sensitivity to short wavelengths (blue and UV), where most of the Cherenkov light is concentrated. Each PMT views the light from a 37 m^2 heliostat so it generates single photoelectrons from night-sky background at a rate in excess of 1.5 GHz. The PMT rapid rise time of 1.5 ns and narrow output pulse width helps to reduce pulse pile-up effects. A small transit time spread of 0.5 ns results in a timing resolution of the experiment of less than 1 ns. Excellent time resolution allows us to exploit the narrowness of the Cherenkov wavefront at the trigger level to reject background from showers produced by charged cosmic rays. Offline, good timing resolution is valuable in reconstructing the shape of the wavefront (approximately spherical) in order to reject background.

The PMTs are supplied with high voltage from LeCroy 4032A high voltage power supplies, which are controlled by a LeCroy 2132 CAMAC interface in the control room. Voltages are typically in the neighborhood of -1600 V. The high voltage values are periodically adjusted to equalize the response of all channels.

E. Front-End Electronics

Fig. 4 shows a block diagram of the STACEE electronics, and Table I summarizes the performance parameters that will be discussed in the following sections.

Signals from the phototubes are filtered and amplified near the cameras before being sent to the STACEE control room, located up to 18 m below the detectors in the tower. There they are discriminated, and used in timing measurements and trigger logic. Concurrently, the analog pulses are continuously digitized.

The front-end analog electronics are physically close to the PMTs. The PMT signals arrive at the front-end electronics via 11 m long RG58 cables. The signals are passed through high-pass RC filters having a time constant of 75 ns. This filter blocks any dc component of the PMT signal and removes slow PMT transients, which are not associated with Cherenkov signals.

The pulsed component of the signals exiting the filters are amplified by two cascaded fixed-gain $(\times 10)$ wide-band (275 MHz) amplifiers (Phillips Scientific 776). This amplification factor of

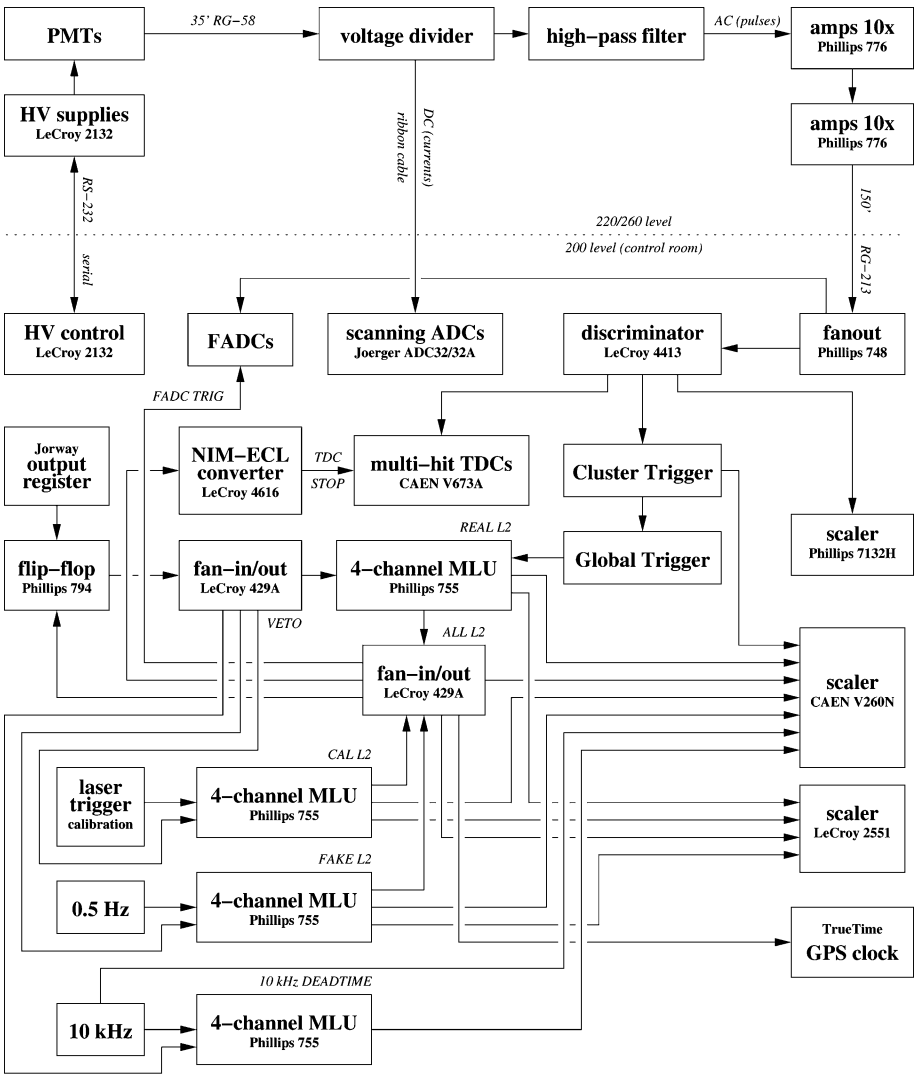

Fig. 4. Block diagram of the STACEE electronics.

TABLE I
PERFORMANCE PARAMETERS OF THE STACEE ELECTRONICS AND TRIGGER SYSTEM

Value	Description
0.5 ns	PMT transit time
1.5 ns	PMT rise time
2000 ns	programmable delay range
1 ns	precision on delay times
1-10 kHz	cluster rates
5 Hz	nominal global trigger rate
15.6 ns	trigger signal jitter
8-12%	trigger deadtime
7.8-23.4 ns	cluster coincidence window
15.6 ns	global trigger coincidence window
140 ns	trigger latency
3.0 ns	minimum pulse width that can be encoded
6 ns	average double pulse resolution
15.6 ns	mean width of double channel coincidence
1 GS/s	FADC sampling rate
8-bit	FADC resolution
1 V	FADC dynamic range
1 ns	experiment timing resolution

100 allows us to keep the PMT gain at approximately 10^5, which is expected to prolong the life of the PMTs in an environment of high night-sky background light levels.

The filtered and amplified signals are routed through up to 40 m of low-loss coaxial cables (RG213) from the detector levels to the control room level of the tower where they are fed into linear fanouts (Phillips Scientific 748). The outputs of these fanouts are passed to the discriminators and flash ADCs (FADCs).

The analog signals from the PMTs are discriminated by 16 channel discriminators (LeCroy 4413 or Philips Scientific 7106) operating with a common threshold. The discriminator thresholds are set according to a rate versus discriminator threshold curve like the one shown in Fig. 5. In this plot, one sees data for in-time delays (empty squares) appropriate for Cherenkov triggers, and random delays (filled squares), which show the contribution from accidental coincidences caused by night-sky background photons. There is a breakpoint in the trigger rate, which is defined as the discriminator threshold below which the rate climbs exponentially. The location of the breakpoint depends on the individual channel rates, the widths of the discriminator pulses, and the number of channels required to form a trigger. At discriminator thresholds below the breakpoint, the rate is dominated by accidental coincidences. At very low discriminator threshold values the curve flattens due to deadtime. At discriminator thresholds above the breakpoint, the rate de-

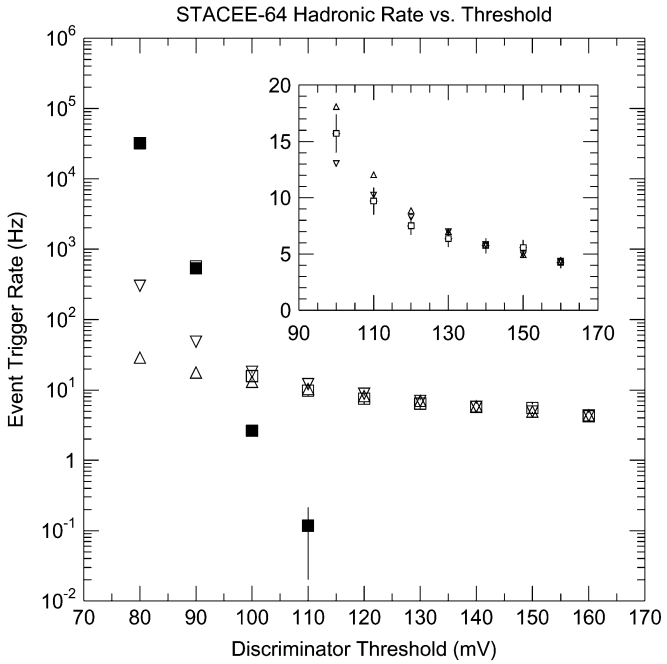

Fig. 5. Trigger rate versus discriminator threshold. The empty squares are data taken with in-time delays and the filled squares for random delays. The triangles are for two simulation models: unit-slope (inverted) and zero-intercept (upright) linear extrapolation. The insert shows the same points above a threshold of 90 mV, with a linear vertical scale so that the error bars are visible.

creases slowly with discriminator threshold for in-time delays where the experiment is triggering mostly on Cherenkov light. The operational discriminator thresholds were set 15 mV to 20 mV above the breakpoint to minimize the background from accidental triggers. Background for STACEE consists almost entirely of hadron-initiated Cherenkov events.

The system should handle PMT discriminator rates up to about 10 MHz. Typical discriminator rates are 1 MHz to 5 MHz. The PMT discriminators contribute an effective deadtime that is rate dependent, and is typically less than 5%.

F. Delay and Trigger System

A unique challenge in STACEE, that led to the design of a custom-built delay and trigger system [7], is the requirement of dynamic delays. Due to the Earth's rotation, the gamma-ray source appears to move across the sky during the course of a night's observations. This effect continously changes the relative arrival times of the Cherenkov photons at each heliostat. In order to maintain tight timing coincidences, signals from different channels are delayed by different amounts to correct for the source movement.

The required range of delay times is determined by the geometry of the heliostat array and the maximum zenith angle at which we observe a source. The programmable delay system has sufficient range (approximately 2 μs) to trigger on Cherenkov showers coming from any region of the sky within a cone of 90° opening angle around the zenith. Individual delay settings can be controlled with a nominal precision of 1 ns. To ensure precise timing, every channel is calibrated with test pulses. The delays are updated every few seconds as STACEE tracks a source across the sky. Typical changes in the delays are approximately 1 ns per 15 s of elapsed time.

STACEE has a two-level trigger system. The 64 heliostats are divided into eight clusters of eight heliostats each (see Fig. 2). The discriminator outputs from the eight channels in each cluster are routed through delays programmed to bring in-time hits into coincidence.

The number of coincident PMTs in a cluster, and the number of coincident clusters, are chosen to optimize the quality factor for the rejection of hadronic air showers according to Monte Carlo simulations. The discriminator threshold is then set at a level which makes the overall event trigger rate from chance coincidences due to fluctuations in the night-sky background photons negligible (less than 0.2 min^{-1}).

Typical trigger settings are a discriminator threshold of 140 mV (about 5.5 photoelectrons), five out of eight PMTs are required to form a cluster trigger, and five out of eight cluster triggers are required to form a global trigger. At these trigger settings Cherenkov events are recorded at a rate of about 5 Hz for offline analysis. Typical cluster trigger rates are 1 kHz to 10 kHz. The precise width of the cluster coincidence window as applied to a given series of pulses varies between 7.8 ns and 23.4 ns due to the implementation of the trigger logic [7]; the mean width for a double-channel coincidence is 15.6 ns. The coincidence window for the global trigger is 15.6 ns. The rate of false triggers, due to spurious coincidences of night-sky background light, decreases dramatically as the coincidence window is made shorter. The physical limit of the coincidence window is given by the intrinsic arrival-time width of the Cherenkov wavefront of about 4 ns.

A by-product of the two level trigger system is that the light pool is required to be spread out over the entire heliostat array. This feature is typical for showers induced by gamma rays and is used to distinguish them from showers initiated by charged cosmic rays.

The rate of accidental triggers due to random night-sky hits in the PMTs can be directly determined by using random settings for the programmable delays (Fig. 5), which in effect is like pointing the heliostats in random directions.

The global coincidence triggers are combined with free running trigger signals generated at a rate of 0.5 Hz. Free running triggers are used for determining individual channel rates and pedestal values. Whenever either type of trigger occurs (coincidence or free running), a common stop signal is sent to latch a GPS clock time and initiate the event read out. During readout, a veto is asserted to prevent the occurrence of additional triggers. The veto is cleared by the data acquisition (DAQ) program at the conclusion of readout.

G. Implementation of the Delay and Trigger System

The STACEE delay and trigger system digital logic circuit is based on Altera FLEX 10 KE embedded programmable logic devices. The system consists of 10 boards in VME format: one clock distribution board, eight 8-channel cluster trigger boards, and one global coincidence trigger board. The system makes extensive use of TTL signals. The only ECL components are ECL/TTL translators, used to receive the input signals from the

discriminators, and to receive and transmit signals between the cluster trigger boards and the global trigger board.

1) Clock Board: The delay and trigger system is a synchronous digital logic circuit except for the tapped delay lines at the inputs. The system clock is generated by a separate clock board containing a 32 MHz TTL clock oscillator. The clock is distributed over the SERCLK line on the VME bus to the nine other boards in the system. Each of these boards uses the SERCLK to synchronize two local phase-locked loop chips to generate 128 MHz and 64 MHz clocks.

2) VME Interface: All communication with the system is over the VME bus. The boards are started and stopped by writing to a control register on each board. The programmable delay values are written to the boards by first selecting the channel to receive the data and then writing to that channel's delay register. The delay specified for each channel can be changed in real time with the system running, as long as the change in the delay value is less than 15.6 ns from the previous value. The programmable delay register can not be read. The trigger conditions are set by writing the multiplicity requirement and coincidence mode to a register on each board. After a global coincidence trigger is issued, the timing information for each channel for the 31.25 ns period preceeding the trigger can be read. In addition, control, status, and test registers are readable and writable.

3) Time Encoding Logic: The differential ECL signals from the discriminators are converted to single-ended TTL signals on each cluster trigger board. An Altera MAX 700 complex logic device (EPM7032) is used to select eight inputs corresponding to a unique set of heliostats from the 16 inputs on the board.

The 128 MHz clock frequency allows for only a resolution of 7.8 ns in the delays. To obtain approximately 1 ns resolution in the delays, tapped delay lines are used in front of the purely digital circuit. Monolithic 10-tap fixed delay lines (3D7110) from Data Delay Devices are used. The tap-to-tap delay of these lines is (1.0 ± 0.5) ns. The input to the first tap delay will lead to an average 1 ns common delay on all channels which just adds to the trigger latency. The constant channel-to-channel variation of this initial delay can be measured and corrected for by including them in the relative programmable delay values.

The time encoding logic runs in a EPF10K30E embedded programmable logic device at a clock frequency of 128 MHz. The lower eight tap outputs are latched every 7.8 ns. As the resulting bit pattern is not synchronous with the 128 MHz clock, a four stage pipeline follows the input flip-flop to recover from metastability. By examining the pattern of bits it is possible to determine the rising edge of the TTL input pulse relative to the previous clock edge. Each 7.8 ns, when the taps are latched, the time can be coded into 3 bits which we call a vernier code. To determine the rising edge of the input pulse, five consecutive tap values are examined for a pattern—two or more zeros followed by at least three ones—that is consistent with the minimum pulse widths and double-pulse resolutions of the 3D7110 tapped delay lines, and the LeCroy 4413 or Philips Scientific 7106 discriminators. Since the input pulses are not synchronized with the clock, the 5-bit pattern can occur across a clock edge so the tap outputs from three consecutive clock periods must be examined to unambiguously determine the hit pattern and its preceeding clock edge. If a valid hit pattern is detected, a fourth bit is set and added to the 3-bit vernier code. The time encoding has a minimum latency of approximately 47 ns. The minimum pulse width that can be encoded is approximately 3.0 ns. The average double-pulse resolution is approximately 6 ns. Pulses separated by 8 ns will be resolved with full efficiency.

4) Delay Logic: Since the asynchronous arrival times of the input pulses are time encoded, the input signals are not delayed but rather the vernier codes are delayed in first-in first-out (FIFO) memories, Since the vernier codes span a range of 8 ns, the FIFO memories should be clocked at 125 MHz. As this was rather fast for field programmable gate arrays available at the time, we choose to multiplex the vernier codes into an EPF10K100 embedded programmable logic device clocked at 64 MHz. In order to synchronize the two programmable logic devices clocked at different frequencies, the 4-bit vernier codes produced by the EPF10K30 are split into two separate paths on alternate 128 MHz clock rising edges, and then resynchronized at 64 MHz, as 8-bit vernier code pairs.

The value of a 7-bit reference counter, in the clock cycle in which the vernier code pair would be pushed onto the FIFO memory, is appended to the vernier code bits. This produces for each 15.6 ns clock period effectively two 11-bit time stamps sharing the same reference counter value, including two code validation bits corresponding to the 0 to 7 ns range and the 8 ns to 15 ns range of the input pulse arrival times.

The time stamp must now be delayed in the FIFO memory for a specified time given by the value in a programmable delay register. For each channel, the content of its programmable 11-bit delay register is combined with the time stamp to produce the delay-time stamp. The delay-time stamp is pushed onto a FIFO memory embedded in the EPF10K100. There is one FIFO memory for each of the eight channels. The upper seven bits of the delay-time stamp of the next available output data in the FIFO memory is compared continously with the reference counter. When there is a match, the vernier codes of the current delay-time stamp are popped from the FIFO memory and inserted into a coincidence pipeline. In this way, each hit for a channel is kept in the corresponding FIFO memory for a period equal to the programmed delay register. The FIFO memory is 2000 ns deep.

Each time the vernier codes are inserted into the coincidence pipeline the vernier codes from the next delay-time stamp are also inserted into the coincidence pipeline. In this way there is 31.25 ns of vernier code information available in the pipeline from which to form the cluster trigger decision.

5) Cluster Trigger Logic: The cluster trigger logic inspects the vernier codes of the eight channels and looks for a coincidence within a selectable time window. The cluster trigger coincidence logic has two different modes of operation: a wide-coincidence mode and a narrow-coincidence mode. In wide mode, a hit anywhere in the first 23.4 ns interval starting at the edge of the 64 MHz clock—that is, within the first three 4-bit vernier codes, each covering one 7.8 ns interval—is considered to be in the coincidence window. A cluster trigger is produced if the number of channels which have such a hit is greater than or equal to the required cluster multiplicity value stored in the multiplicity register on the cluster trigger board.

In narrow-coincidence mode, a coincidence window slides through the vernier codes in 1 ns increments, starting at the 64 MHz clock edge, and a cluster trigger is produced if the number of channels with at least one hit in this window exceeds the multiplicity requirement set in the multiplicity register on the cluster trigger board.

The width of the coincidence window for narrow-coincidence mode is fixed. It can be changed by modifying the EPF10K100 circuit and reloading the configuration file. At present the narrow-coincidence mode window width is 12 ns. If the coincidence window is larger than 7.8 ns, a channel can have more than one hit within the coincidence window.

The cluster trigger signal is synchronized with the 64 MHz clock and fed to the global trigger board for the duration of one clock period. The cluster boards also provide NIM pulses on the front panels, which are counted by a VME scaler (Caen V260N).

Because of the latency associated with transferring the cluster trigger signals to the global trigger boards, the cluster trigger boards do not stop if a local cluster trigger is asserted. Instead, they keep the vernier hits in a pipeline and only stop upon reception of a "hold" signal from the global coincidence trigger board. If the hold signal is received, the vernier hits for the last 31.25 ns are extracted from the coincidence pipelines and made available for readout. The overall trigger latency is approximately 140 ns.

Notice that the cluster trigger logic is performed every 15.6 ns, although it uses up to 31.25 ns of vernier code information. Thus there is some redundancy, and a single "event" can cause consecutive clock cycles to generate cluster triggers. As a result, the cluster trigger output signal is sometimes 15.6 ns wide and sometimes 31.25 ns wide.

6) Global Trigger Board: The cluster trigger information is routed to the global trigger board over front-panel connectors using differential ECL signals. The global trigger logic simply forms the arithmetic sum of the number of cluster triggers it receives within one 15.6 ns clock period. If this sum is equal to or larger than the value in the global trigger multiplicity register, then a global coincidence trigger is asserted.

The assertion of the global trigger generates a hold signal that is fanned out to the cluster boards over front-panel connectors using differential ECL signals. In addition, a NIM-level trigger signal from the global trigger board alerts the DAQ that the event should be read out. At this stage, four 4-bit vernier codes, corresponding to the 31.25 ns period preceeding the global trigger, are extracted from the coincidence pipeline, and read over the VME bus for every board and for every channel. Once all the required information has been gathered, the DAQ software issues a clear-FIFO command to all the cluster trigger boards, and reactivates the trigger by writing into the control register of the global coincidence trigger board.

7) Performance: Since the input pulses arrive asynchronously with respect to the clock, even after the programmable delays are applied, the trigger signal will have a 15.6 ns jitter. The jitter can be corrected for offline by using the vernier time codes of the individual hits.

The coincidence windows are discreet with a 1 ns step. Thus, the coincidence efficiency as a function of the difference in time between two channels is a trapezoid with a base at zero efficiency that is 2 ns longer than the top at 100% efficiency. There are departures from the ideal case due to the fact that the tapped delay lines used for the vernier encoding are not perfect. The broadening of the coincidence resolution relative to the ideal value is significantly less than 1 ns. This includes contributions from all sources of broadening: unequal delay taps, encoding eight 1 ns tap delays in a 7.8 ns clock period, tolerance in the absolute values of the delays, etc.

H. Flash ADC System

To reconstruct the energy and direction of the primary gamma ray, a commercial FADC system made by Acqiris Inc. is used. Sixteen channels of FADCs are contained in a special crate along with their own embedded computer running a version of the Linux operating system, modified to support real-time applications. Four FADC crates make up the system.

Each electronics channel is sampled at 1 GS/s with an 8-bit resolution and dynamic range of 1 V. The zero points of the FADC inputs are calibrated to a precision of 1 mV RMS, and the channel-to-channel gains of the system are equalized to within 0.5%.

The fully digitized PMT waveforms allow not only accurate measurements of the timing and intensity of the wavefront, but also the measurement of the charge-timing correlations, such as the distribution of Cherenkov photon arrival times at each heliostat. This enables us to use various new methods [8], [9] to reject the large background of hadronic events due to charged cosmic rays, while retaining gamma-ray initiated events. The FADCs are also routinely used to calibrate and monitor the gains of the PMTs using a custom-designed laser calibration system.

I. Laser Calibration System

STACEE is equipped with a laser calibration system comprising a 100 μJ nitrogen laser and dye cell feeding a network of optical fibers through a system of adjustable neutral density filters [10]. The fibers deliver light to the PMTs by exciting small diffuser plates attached to the center of the secondary mirrors. The intensity of each laser shot is measured independently using four PIN photodiodes.

The system is used for measuring the relative time differences between PMT channels. It is also used for monitoring gain stability of the PMTs.

The timing resolution is estimated by examining distributions of residuals to shower fits. It is better than 1 ns for all channels and does not depend on the pointing angle. It is stable over time.

J. Miscellaneous Electronics

STACEE uses a GPS clock to provide a time-stamp, accurate to 1 μs, for all recorded events. These time-stamps are necessary for pulsed emission searches.

Counters are used to measure the deadtime due to the readout. Whenever a trigger occurs, a flip-flop is set which asserted a veto signal that inhibits further triggers. This veto is required to prevent additional triggers from interfering with the readout, and it is cleared by the DAQ computer once the readout is complete. A 10 kHz clock is sent to two scaler channels to measure the deadtime. One scaler counts a vetoed copy of the clock and the other counts an unvetoed copy. The ratio of the vetoed scaler

count to the unvetoed scaler count gives the livetime fraction of the experiment. Scalers are also used to monitor the rates of all the discriminated PMT pulses as well as all the cluster triggers.

The cluster trigger deadtime during normal running is negligible. The overall deadtime is dominated by the readout time and varied between 8% and 12% depending on the trigger rate.

K. Data Acquisition

The data acquisition system for STACEE is based on a VME embedded PC which reads out the VME crate and a CAMAC crate via a branch bus. Data are read out after each trigger and stored on a local disk. At intervals, the data are copied from the local disk, along with the FADC data, to a separate PC and eventually written to DLT tape for archiving and off-site analysis. Monitoring in real time occurs on a PC running Linux.

In the NSTTF control room, the positions and motions of the heliostats are monitored and the data are written to disk to be merged with the detector data at the end of observation. In a similar fashion, the weather and atmospheric conditions are monitored and recorded.

III. Detector Modeling

The modeling of STACEE consists of simulating extensive air showers, the optical throughput of the detector, and the electronics. Since STACEE is an atmospheric Cherenkov experiment, the atmosphere is an integral part of the detector.

A. Extensive Air-Shower Simulations

The design and understanding of STACEE is aided by the CORSIKA air-shower simulation package [11]. CORSIKA makes use of packages such as EGS4 [12] and GHEISHA [13], which are widely used in other scientific fields. CORSIKA simulates the entire development of an extensive air shower, starting with the first interaction of the primary particle in the upper atmosphere, and follows all generated secondary particles until they reach the ground or their energy falls below the point where they no longer contribute to shower development. For the energies relevant to STACEE ($E < 10^{12}$ eV) we are able to follow all particles since the multiplicities are small enough.

The intervening processes accounted for by the program include ionization, bremsstrahlung, and pair production, as well as effects such as the deflection by the Earth's geomagnetic field, and Coulomb scattering in the atmosphere.

The development of the shower depends on the density profile of the atmosphere, and thus the assumed atmospheric profile is an important input of the simulation. The rate and angle of production of Cherenkov photons by particles in the shower depend on the local refractive index. In addition, the attenuation of Cherenkov light due to Rayleigh and Mie scattering and absorption by oxygen allotropes are important simulated effects.

B. Optical Simulations

The second part of the STACEE simulation chain traces the optical path of Cherenkov photons through the detector optical elements. For this part, a custom-written ray-tracing package called "sandfield" (Sandia Field Simulator) was developed. Sandfield follows the path of every Cherenkov photon through the optical elements (heliostats, secondary mirrors, and DTIRCs) onto the PMT photocathodes, folding in transfer efficiencies at every stage. The arrival times are smeared with a Gaussian resolution of 0.5 ns width equivalent to the transit time spread of the PMT. The end result is a list of photoelectrons and their arrival times at the PMTs per channel. These lists are passed to the electronics simulator for further processing.

C. Electronics Simulations

STACEE PMTs are bombarded with a high flux of photons either from air showers or from night-sky background light. The elevated rates caused by pile-up effects need to be understood quantitatively, so a detailed electronics simulation package is essential.

The photoelectrons from the air shower (generated by the sandfield program) are combined with random night-sky background photoelectrons generated uniformly in time according to Poisson statistics. A simulated analog waveform is built up by superimposing single photoelectron pulses using an analytical pulse shape and adding them according to their arrival times.

The different gains of the channels are simulated by appropriate scaling of the pulse amplitudes. The waveforms are finally passed through a simulation of the discriminators.

D. Simulation Cross-Checks

In order to verify the simulations, calibration data are recorded and compared with the simulations. CORSIKA was compared to another commonly used extensive air-shower simulation package, MOCCA [14]. The simulations agreed at the 20% level. We have chosen CORSIKA because it simulates the air-shower processes in greater detail, particularly in the simulation of hadronic primaries.

For sandfield, cross-checks have included simulating the sunspot data and the drift-scans of stars. For the electronics simulation, most quantities read out in the real data have been cross-checked, including PMT rates, distributions of FADC trace samples, pulse-height distributions, and the overall trigger rates, as functions of photocurrents, gains, discriminator thresholds, etc.

A powerful check of the simulation is to reproduce the absolute rate versus threshold curves for various PMT channels. The PMT rate at low threshold is due to the random pile-up of single photoelectrons exceeding the discriminator threshold. It is directly related to the photocurrents, both quantities depending on the single photoelectron rate, the PMT gain, and the average pulse width. Small variations in any of these quantities produces large changes in the rate. Thus, reproducing actual rate versus threshold curves is a sensitive test of the validity of the simulation, particularly the calibration of the discriminator threshold level in terms of photoelectron equivalents. This calibration directly affects the gamma-ray energy threshold calculation.

Fig. 5 shows a comparison of these simulations with a real-data rate versus threshold curve. The simulations are clearly inaccurate below a threshold of 100 mV. However, this is approximately the point at which accidental coincidences begin to dominate the event trigger rate, as is visually apparent by the sharp break in slope. Since the simulation does not currently support a

mode which can trigger on night-sky background as well as simulated Cherenkov showers at the same time, it is unrealistic to expect it to simulate these points correctly. However, at thresholds of 100 mV and above, the simulations perform quite well.

A good end-to-end test of the simulation chain is the calculation of the rate due to cosmic-ray triggers. The cosmic-ray spectrum in the energy range relevant to STACEE is well known. Cosmic-ray data are obtained by collecting showers from the zenith. Many cosmic-ray runs are taken by STACEE so a comparison between calculated and measured cosmic-ray rates is straight-forward. A comparison of real versus simulated hadronic cosmic-ray event rate for several detector headings (hour angles) agree to 5% or better [15].

Although past published results from STACEE include only integral fluxes, more information can be extracted from the measured charges and arrival times of the PMT pulses associated with the Cherenkov wavefront. These event reconstruction techniques have been tested only in simulations. Although much work remains to be done, the most realistic simulations performed to date show great promise in the new reconstruction techniques [15]. The shower-core resolution is 10 m, independent of energy for all showers with energies between 300 GeV and 2 TeV. The energy resolution is about 20% if the core is known to within 10 m of its actual location.

IV. Summary

STACEE is a complete ground-based Cherenkov wavefront sampling gamma-ray telescope using heliostat mirrors of a solar energy research facility. Cherenkov light from air showers generated by the impact of high-energy gamma rays on the upper atmosphere is collected with a set of 64 heliostats with a collective area of over 2300 m^2. To date STACEE has achieved a low-energy threshold of about 100 GeV, which is lower than previously obtained by ground-based imaging detectors. Since the complete detector came into operation in spring of 2002, the measuring time was spent for observations of the Crab nebula, the active galactic nuclei 3C66A, OJ+287, W-Comae, Markarian 421 and H1426, and five gamma-ray bursts.

A modification to the STACEE electronics system during the summer of 2004 to move the FADC system closer to the PMTs and to install new high-gain pre-amplifiers at the PMTs will allow STACEE to operate with a faster, cleaner, electronic system at a lower energy threshold during the upcoming seasons.

Acknowledgment

The authors are grateful to the staff at the National Solar Thermal Test Facility for their excellent support.

References

[1] R. C. Hartman *et al.*, "The third EGRET catalog of high-energy gamma-ray sources," *Astro. J. Suppl.*, vol. 123, pp. 79–202, Jul. 1999.
[2] D. S. Hanna *et al.*, "The STACEE-32 ground based gamma-ray detector," *Nucl. Instrum. Meth.*, vol. A491, pp. 126–151, Sep. 2002.
[3] M. de Naurois, "Measurement of the Crab flux above 60 GeV with the CELESTE cerenkov telescope," *Astro. J.*, vol. 566, pp. 343–357, Feb. 2002. CELESTE Collaboration.
[4] S. M. Tripathi *et al.*, "The Keck solar two gamma-ray telescope and its observations of the Crab Nebula," in *Proc. ASS 200th Meeting, 25.03*, Albuquerque, NM, June 2002, p. 676.
[5] F. Arqueros, "The GRAAL experiment," in *Nucl. Phys. B-Proc. Suppl.*, vol. 114, Feb. 2003, pp. 253–257. GRAAL Collaboration.
[6] X. Ning, R. Winston, and J. O'Gallagher, "Dielectric total internal reflecting concentrators," *Appl. Opt.*, vol. 26, pp. 300–305, Jan. 1987.
[7] J.-P. Martin and K. Ragan, "A programmable nanosecond digital delay and trigger system," in *Proc. IEEE NSS/MIC Conf.*, vol. 2, Lyon, France, Oct. 2000, pp. 12/141–12/144.
[8] R. A. Scalzo, "Optimized pointing strategies for solar tower ACTS," in *Proc. 28th International Cosmic Ray Conference, OG 2.5*, Tsukuba, Japan, Jul. 2003, pp. 2799–2802. STACEE Collaboration.
[9] J. Zweerink, "Using GHz FADC's to reject hadrons from STACEE data," in *Proc. 28th International Cosmic Ray Conference, OG 2.5*, Tsukuba, Japan, Jul. 2003, pp. 2795–2798. STACEE Collaboration.
[10] D. Hanna and R. Mukherjee, "The laser calibration system for the STACEE ground-based gamma ray detector," *Nucl. Instrum. Meth.*, vol. A482, pp. 271–280, Apr. 2002.
[11] D. Heck, J. Knapp, J. N. Capdevielle, G. Schatz, and T. Thouw. (1998) CORSIKA: A Monte Carlo Code to Simulate Extensive Air Showers. [Online]. Available: http://www-ik.fzk.de/~heck/corsika/
[12] W. R. Nelson, H. Hirayama, and D. W. O. Rogers, The EGS4 Code System SLAC-0265, Dec. 1985.
[13] H. Fesefeldt, "GHEISHA, the Simulation of Hadronic Showers: Physics and Applications,", RWTH Aachen Report PITHA-85/02, 1985.
[14] A. M. Hillas, "Ground-based gamma-ray astronomy," *Nuovo Cim. C16*, pp. 701–712, 1996.
[15] R. A. Scalzo, "Observations of the EGRET Blazar W Comae with the Solar Tower Atmospheric Cherenkov Effect Experiment," Ph.D. dissertation, Univ. Chicago, Chicago, IL, 2004.